Using a Maxwell's demon to orient a microsphere in a laser trap and initiate thermodynamic assays of photonic nanofields

Vaclav Beranek[a], Igor R. Kuznetsov[b], Evan A. Evans[b*]
[a]Bioengineering, Georgia Inst. of Technology, Atlanta, GA, USA 30332; [b]Biomedical Engineering, Boston University, Boston, MA USA 02215

ABSTRACT

Seeking to control free rotations of a microsphere in a laser trap, we have created a "Maxwell's demon" that identifies and captures a preferred "up-or-down" polarity of the microsphere. Breaking rotational symmetry, we attach a single "Raleigh-size" nanoparticle to a micron-size sphere, which establishes a "nanodirector" defining microsphere orientations in a trap. With radius <10% of the NIR trapping wavelength (1.064 μm), a polystyrene nanoparticle appended to a ~1.3 μm glass sphere adds negligibly to scattering of the trapping beam and imperceptibly to forces trapping a doublet probe. Yet, constrained to a large orbit (~1.5 μm diameter), the weak Raleigh dipole force induced in the nanoparticle imparts significant pole-attracting torques to the probe. At the same time, Brownian-thermal excitations contribute torque fluctuations to the probe randomizing orientations. Thus, we have combined demon control and Boltzmann thermodynamics to examine the intense competition between photonic torques aligning the nanodirector to the optical axis and the entropy confinement opposing alignment when equilibrated over long times for an order of magnitude span in laser powers. To reveal orientation, we developed novel multistep pattern-processing software to expose and enhance weak-diffuse visible light scattered from the nanoparticle. Processing a continuous stream of doublet images offline at ~700 fps, the final step is to super resolve the transverse XY origin of the scattering pattern relative to the synchronous probe center, albeit limited to "up" state segments because of intensity. Transforming the dense histograms (~10^4-10^5) of radial positions to polar angle (θ) distributions, we plot the results on a natural log scale versus sin(θ) to quantify the photonic potentials aligning the nanodirector to the optical axis. Then guided by principles of canonical thermodynamics, we invoke self-consistent methodology to reveal photonic potentials in the "down" state.

Keywords: photonic nanotools, statistical mechanics of small systems, Brownian dynamics, optical trapping

1. INTRODUCTION

Maxwell's "demon"[1] has long been viewed as a provocative thought experiment to challenge the second law of thermodynamics. Yet in recent times, the demon has been rebranded and promoted as an innovative tool for advancing nano-science and nano-technology. Often central to demon design, symmetry breaking is used to structure unique nano-states providing a means to switch or enable feedback between states[2-4]. For instance, breaking circular symmetry, optical and magnetic traps have been shifted from one location to another to transport small particles and even verify thermodynamic principles.[5-7] Similarly, breaking rotational symmetry, birefringent and aspherical micro particles have been used in laser traps as variable-speed rotators to assay viscous damping in fluid environments – and even quantum friction in vacuum.[8-12] While many manifestations of symmetry breaking produce non-equilibrium systems, the outcome can be steady states with special dynamical properties yielding concepts for unusual nanomachines.[4] By comparison, we show that using a weak perturbation to break rotational symmetry of a microsphere probe leads to equilibrated patterns of orientations if held in a trap for sufficient time at constant power. At the same time, we show that demon design and operation benefit significantly from the spontaneous break in "up-down" mirror symmetry of a trapped sphere. Well known, the photon pressure created by laser scattering displaces the probe center outward from the trap focus.[13-17] Thus, parameterized by input power, separate branches of equilibration emerge from two symmetry breaks to describe the minimal free energy landscape governing orientations. Combined with offline nanoparticle pattern processing, we demonstrate that thermally equilibrated distributions of probe orientation provide photometric tools to assay the laser intensity field local to the probe, determine small mis-alignments of the optical axis, and implement demon software targeting specific nanostructures against a surface.

*evanse@bu.edu phone | 617 669-5620

2. EXPERIMENTAL METHODS AND RESULTS

2.1 Doublet selection and trapping

Employing Brownian imaging methods established previously[18], we began the ~20 hour series of experiments described in this work by selecting a ~1.3 μm probe at random from a sample preparation in containing 1-2 μm size particles, which we demonstrate below to be a doublet. Given the uncertainty in dimensions, each micron-size probe is unique and the software parameters used to track the probe with auxiliary visible light must be calibrated *in situ*[18] (i.e. 0.15 M NaCl). Once accomplished, the tracking software reports 3-d displacements of the probe angle-averaged center position on line at ~80 fps (offline at ~700 fpc) with nm precision (e.g. SD ~ ± 2 nm for transverse ΔX, ΔY and SD ~ ± 4-5 nm for height ΔZ displacements when stationary). In Fig. 1A, we illustrate the 3-d tracking and trap calibration by superposing a sequence of center positions obtained for the doublet at constant input power. In Fig. 1B, we show Z-tracking under demon power control that confirms the doublet configuration.

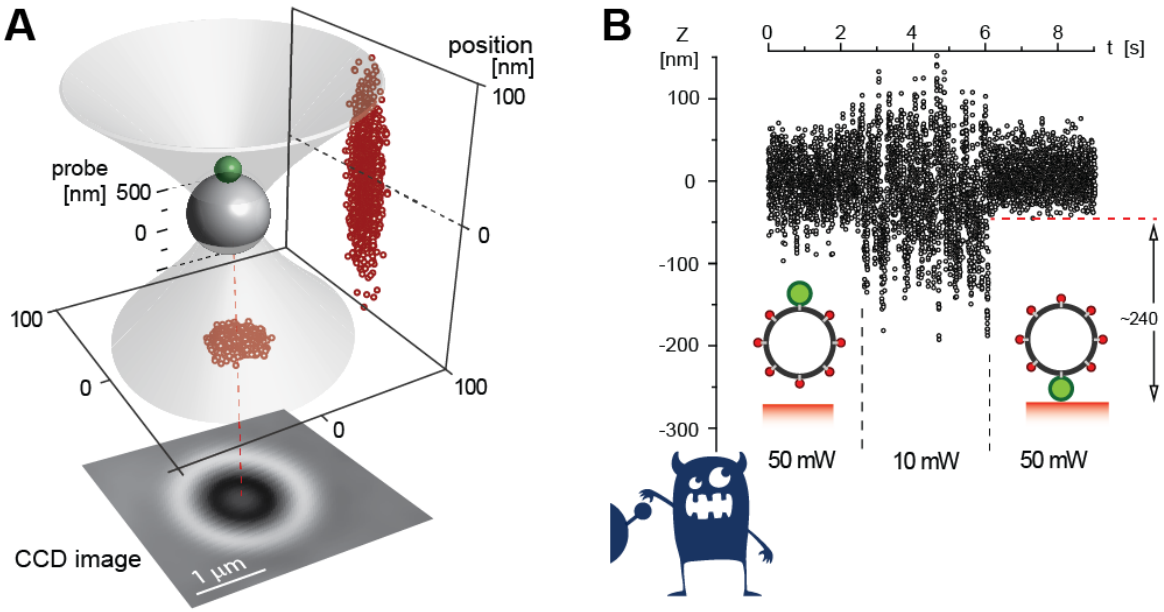

Figure 1. A. Image of the free energy potential trapping the micron-size doublet when elevated 1 μm above the cover glass trap window. Bare positions of the probe obtained at a power of 50 mW are shown projected onto 100 nm x 100 nm XY and XZ planes. Tracked offline at ~700 fps, this subset of positions (~10^4) forms a distinct cigar-like harmonic shape in the trap – albeit "cropped" all-around by motion blur.[18] Also sketched in perspective is the polystyrene nanosphere linked to a borosilicate microsphere (doublet) drawn to putative scale; below is a centered CDD image in the XY plane. B. Z tracking of the probe under demon control after reduction in elevation to ~270 nm separation. The sequence shows a switch in orientation from "up" to "down" polarity of the nanoparticle. Beginning with capture of the doublet in an "up" polarity at 50 mW, the demon switches to passive observation of frequent "up-down" exchanges at 10 mW, then returns to 50 mW to capture the doublet in a "down" polarity as evidenced by strong steric exclusion of fluctuations below ~50 nm separation. [Note as shown by fast position tracking in A at 1 μm separation, the fluctuations in Z trapping potential span about 3-4 SD (≈±23nm) at 50 mW whereas at ~80 fps in B (left), motion blur reduces the span to ~2-3 SD and similarly for fluctuations at 10 mW where SD ≈ ± 51nm.[18]].

Although not required in the thermodynamic analysis to follow, the three Gaussian distributions describing thermal fluctuations in Fig. 1A must be corrected for motion blur to provide the actual "spring constants" characterizing the 3-d harmonic potential.[18] Evaluated in this way at eight laser powers ranging from 10 to 75 mW, the doublet spring constants are found to correlate linearly with laser beam power Pwr as given by, $\kappa_\perp$ /Pwr ≈ 0.00076 pN/nm/mW for lateral confinement and $\kappa_\parallel$ /Pwr ≈ 0.00016 pN/nm/mW for vertical confinement. Importantly, following offline image processing at ~700 fps, we failed to detect measurable cross correlations between nanoparticle radial positions and the ΔX, ΔY, ΔZ translational displacements of the doublet at any power. Hence, consistent with the Raleigh-particle idealization, we treat the potential energy landscape governing orientation as essentially independent of translational.

Footnote[1]: the input powers referred to in units of mW (**Pwr**) are apparent values reported by a laser power controller positioned in the beam line prior to imaging by the microscope optics. Thus, to better estimate the trapping power, we have determined the scale factor needed to match the regressions for axial and transverse spring constants ($\kappa_\parallel$, $\kappa_\perp$) per unit Pwr with accurate calibrations of actual trapping power in mW. Choosing the detailed results published by Mahamdeh, Campos, and Schäffer[17], we estimate that the actual doublet trapping power in mW should be ~0.44 **Pwr**. Likewise, comparing our ratio for $\kappa_\perp$ / $\kappa_\parallel$ = 4.8 to their results indicates that the filling ratio for our laser beam entering the at all powers objective was likely to be ~0.7. Well appreciated, the value of filling ratio allows the beam waist at the trap focus to be estimated as examined in several excellent theoretical articles[13-15] and described in a seminal review[16].

2.2 Demon design and operation

To implement demon detection, we continuously sample the central-zone intensity of each probe image during position tracking. Defining the sample, M_Σ is the total visible-light intensity cumulated within a 294 nm (15 pix ⇒ 19.6 nm/pix) distance from the probe center (cf. images in Fig. 2B), which appears as the fluctuating gray signal in Fig. 2C. Monitoring a ~41 point moving average of the cumulate, we achieve ~97% or better fidelity in demon detection during online operation. Identified online 3-4x faster than the characteristic time (~1 s) for free diffusive rotations, an "up" step in brightness detects presence of the nanoparticle traversing the hemisphere illuminated directly by visible light, whereas a "down" step detects presence on the opposite hemisphere illuminated by weaker light passing through the microsphere (cf. sketch in Fig. 2A). [Juxtaposed to the imaging light by epi-illumination, the "down-and-up" hemispheres are also illuminated by convergent-and-divergent NIR light entering-and-exiting the trap respectively.] To capture and verify transition events, the demon inserts ~2s steps to high power (e.g. 100 mW), which pin the metric to discrete levels characterizing confinement close to the "up" pole (green segment in Fig. 2C) or to the "down" pole (red segment in Fig. 2C). Also shown in Fig. 2C, a 100 point moving average superposed on the gray signal highlights the abrupt 2s-steps verifying recognition. As described later, a demon 2s step at 100 mW was used to initialize the origin for Brownian rotational relaxation local to the "up" pole when followed by a switch to lower power.

Examining long-time trajectories at low laser input powers (≤ 15 mW), we used demon tracking to construct "bit-level" maps (Fig. 2D) exposing the random occupancies in each "up-down" region during global equilibration. Plotted on a descending log scale of statistical frequency $[N(t_i)/N_{total}]$, occupancy times in the "down" and "up" regions are found to exhibit single exponential decay (cf. $\log_{10}$ example in Fig. 2E at 10 mW). Calculating the ratios of mean occupancy times (e.g. by linear regression to each natural log decay), we obtain statistical estimators for the probability ratio (P_D/P_U) defining the free energy difference between "down-up" regions, i.e. ~ $k_BT \ln(P_D/P_U)$. Found to increase linearly with power, $\ln(P_D/P_U)$ revealed a dramatic power-dependent preference for "down" versus "up" regions [cf. black dotted line in Fig. 2F], which originates from the spontaneous break in mirror symmetry driven by probe scattering of the the trapping beam. Supporting the demon estimate after detailed processing of nanoparticle scattering patterns, the final ratios for (P_D/P_U) are shown plotted as open circles (±SDs) along with their linear regression (solid blue line in Fig. 2F) yielding, $\ln(P_D/P_U) \approx 2.66$ (Pwr - 7.0). Clearly unlike the zero-power intercept found for trap spring constants, the free energy difference between "down" – "up" orientations was found to vanish at ~ 7 mW power.

Footnote[2]: In an attempt to evaluate a power lower than 10 mW, we obtained the bit map data at 8* mW with a second doublet chosen after completing the full set of experiments with the primary doublet. The second doublet was slected to be close in size to the first doublet. For both doublets at very low power, extreme fluctuations in position threatened to expel each probe from its trap and roughened the pattern of orientations found to correlate distributions from 15 to 100 mW.

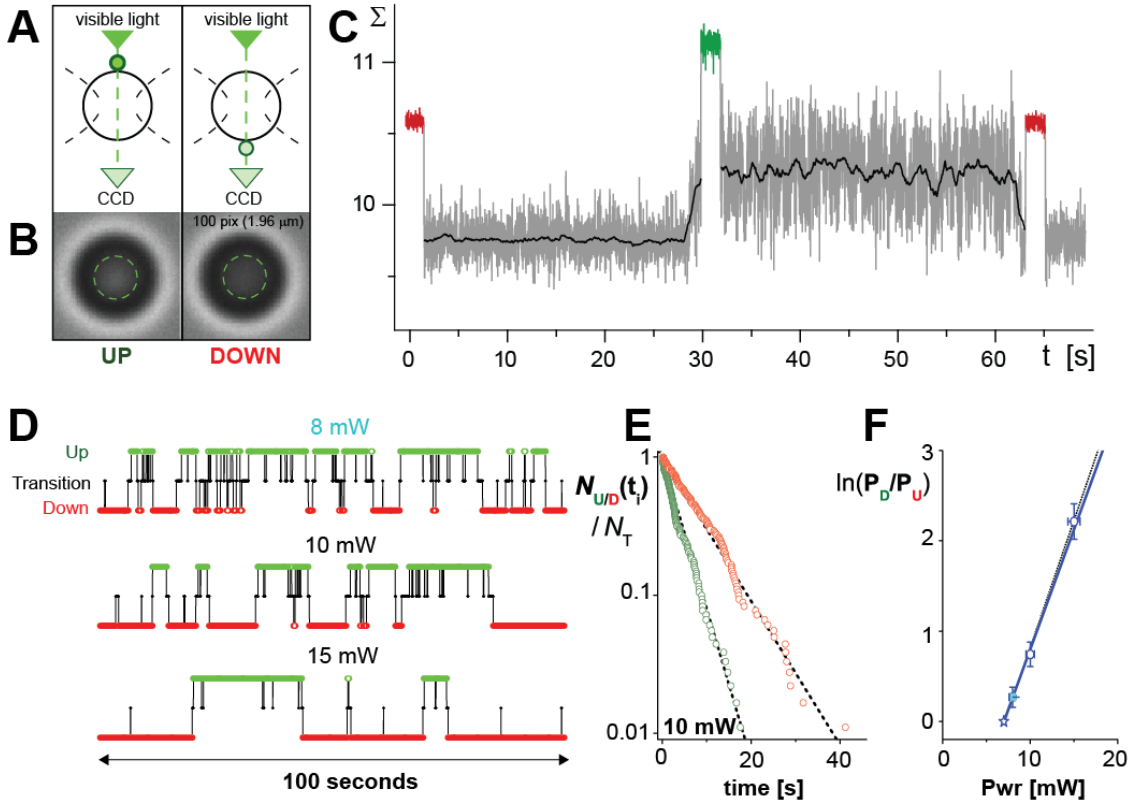

Figure 2. Demon tracking of "up" - "down" nanoparticle excursions online at ~80 fps. A. Schematics of visible light image formation. B. Actual CCD images at 100 mW below show the central zone of intensity (dashed circles) evaluated by demon detection. C. Traces of the bare intensity metric (gray) and a moving average (black line) demonstrate transitions from "down" to "up" to "down" at 10 mW, punctuated by 2s steps to 100 mW power. The steps were inserted by the demon to verify recognition (red level = "down" and green level = "up"). D. Three-level bit maps acquired online from 41 point moving averages of the bare intensity matrix during global equilibrations at low laser input power (8*, 10, 15 mW). Again, red-green levels report detection of the nanoparticle in "down"-"up" regions. Black intermediate levels in D also identify brief transitions (average ~ 0.36 s) and occasional failed attempts. E. Occupancy times (in descending order of frequency) are shown plotted on a $\log_{10}$ scale versus time for "up" (green) and "down" (red) bit levels acquired at 10 mW. As shown by E, single exponential decays were observed for all three low powers. Thus, the estimators for "expected occupancy times" were derived from slopes of linear regressions to the data sets for all three powers on a natural log scale. Taking each "down"/"up" ratio of occupancies as the estimator for probability ratio (P_D/P_U), the regression summarizing bit-map assay of $\ln(P_D/P_U)$ at low powers appears in F as a dotted black line. Also plotted in F, open circles (bracketed by standard deviations) show the final 3-state statistics used to characterize the probability ratio. The solid-blue line in F is the regression line fitting the open circle data (open-blue star marks its origin at $P_D/P_U = 1$).

2.3 Nanoparticle position analysis and nanodirector orientation in the "up" state

We employ multistep pattern processing to track nanoparticle locations in doublet images streamed offline throughout each experiment at ~700 fps. Prior to pattern analysis, XYZ center-tracking software[18] is applied to the full sequence of raw images, shifting each XY doublet-image center to a common-synchronous origin. Next, an array of average images are computed for a range of doublet Z values (elevations) and stored. Once accomplished, pattern processing commences by selecting the average image appropriate to a current doublet elevation and subtracting it from the centered raw image to expose the weak-diffuse visible light scattered by the nanoparticle. This step is then followed by application of a median filter to reduce noise and finally, a gradient filter to enhance the scattering pattern. Seen overlaid on an irregular-dark background in Fig. 3A (top-right), the gradient-processed pattern is distinguished by a prominent "donut-like" feature with a small-dark center when directly illuminated by incident visible light. Thus, compelled by the shape, we convolve a circular donut "mask" of comparable size (Fig. 3A, top-left) with the bright feature, maximizing the convolution with respect to variation in position to establish the nanoparticle location (small-red cross in Fig. 3A, bottom-right).

Organized into a 2-d histogram for each power, we determined the number of nanoparticle positions projected onto each $\Delta X \Delta Y$ image pixel (19.6 nm x 19.6 nm). Coarse-graining the dense histograms of ~10^4-10^5 positions into ~10-40 contour levels, we obtain nested quasi-circular contours with a most probable center position slightly displaced from XY origin as shown in Fig. 3B. Recognizing each contour to represent an annulus of positions on a spherical orbit, we need to specify the orbit radius R_o in order to transform XY histograms to distributions of nanodirector orientations, as described by polar angles (θ,ϕ) relative to the optical axis. Exposed by the small offset in most probable center position relative to the XY origin, we also need to account for a small mis-alignment between the optical axis and the vertical Z axis. Fortuitously, the choice of orbit radius is constrained by compatibility between mis-alignment of the optical axis and the offset in most probable center position, providing a direct way to estimate the oribit radius. Even so, statistical variations in most probable center location from test-to-test require that the radius value be obtained by minimizing the errors in compatibility over all powers tested.

To specify orientation of optical axis, we compute the moment of inertia tensor characterizing shape of the trapping potential in XYZ coordinates (cf. Fig. 1A) and determine the principal axis vector aligned with its long symmetry axis. Shown emerging from a scaled image of the trapping potential inside a micron-size sphere, the principal axis vector (red line in Fig. 3C) was found to tilt slightly (~7^o) from the vertical Z axis normal to the XY plane (black, green, blue lines in Fig. 3C). Scaled by orbit radius, the optical axis intersects the orbit at a location, which first moves toward then away from the most probable center position as radius increases. Thus, we optimized the orbit by finding the radius value that minimized closest approach to all of the most probable center positions. Only evaluated for tests of the primary doublet, the optimal orbit radius was calculated to be ~740 nm (SEM±80 nm). Based on a 740 nm radius, the dense matt of open green circles in Fig. 3C shows ~10% of the nanoparticle locations acquired at 40 mW (Fig. 3B) mapped to the orbit. A semi-transparent (100 nm radius) hemisphere represents the nanoparticle at its most probable position close to the "up" pole.

Circularly averaged to smooth out small irregularities, a MLE routine was used to establish azimuthally symmetric polar angle distributions for the eight tests at powers from 10-100 mW. Varying with test duration and power, the dense distributions contain ~10^4-10^5 nanodirector orientations. Plotted on a $\log_{10}$ scale versus $\sin(\theta)$ in Fig 3E, we show polar angle distributions for three powers (15, 20, 40 mW) normalized to densities. Along with power level, the important distinction between the distributions is that they represent two different types of equilibration experiment. First, to test global equilibration, the experiment required frequent transitions between "down" and "up" hemispheres, which could only be accomplished at powers ≤ 15 mW (cf. Fig. 3E, 15 mW distribution). Even then, each test lasted a few minutes . As shown by Fig. 2F, just doubling the power would increase the testing time tenfold. Thus, a second type of test was configured to examine Brownian equilibration confined by strong "up" state potentials at input powers from 20-75 mW. Limited to ~75s duration for powers from 20-75 mW, the Brownian relaxation would not allow a single nanoparticle trajectory to reach the "down" state region. However, to insure uniformity of the approach, we used the demon to initialize an "up" polarization by a 2s pulse at 100 mW, then switch and hold power to a lower level for 75s.

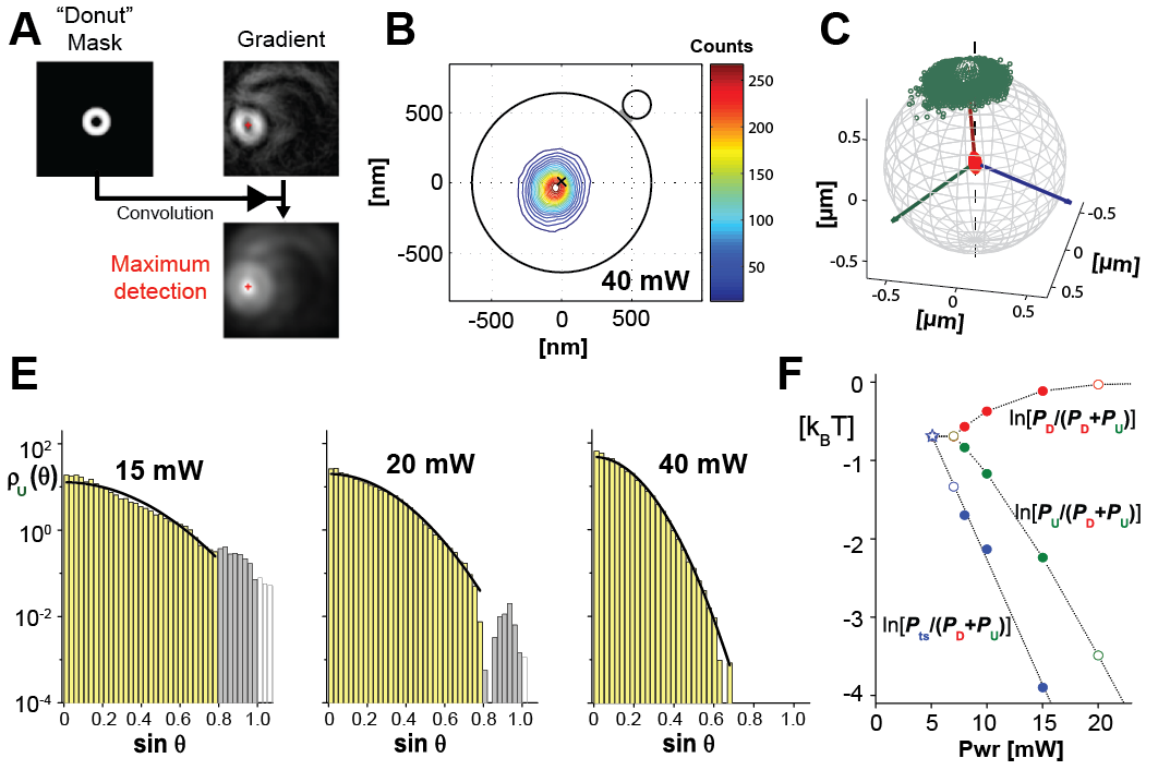

Figure 3. A. Final stage of multistep pattern processing used to track nanoparticle location in centered fast-frame (~700 fps) images. (Top right image) Gradient filtered image obtained after subtraction of a relevant average image then a median filter to remove noise (cf. text). This final enhancement of the weak pattern of scattered light reveals a prominent "donut-like" feature with a small-dark center. (Top-left imag) Circular mask used to super resolve prominent "donut-like" features in gradient filtered images. (Bottom-right image) Optimal convolution with the prominent feature following variation of the mask position, which defines nanoparticle location (small-red cross). B. Profile of the doublet geometry overlaid by contours of nanoparticle position tracking at 40 mW. Defining the contour levels, the color scale at right indicates number of positions counted in an annular-orbit slice. C. Graphic 3-d image showing the glass microsphere depicted as a ~640 nm radius wire-frame mesh. Mapped to a concentric orbit (radius ~740 nm), ~10% of positions obtained at 40 mW appear superposed as open green circles surrounding a semi-transparent hemisphere (radius 100 nm) placed the at the nanoparticle most probable location. Centered inside the wire-frame sphere, the doublet trapping statistics from Fig. 1A are reduced to a red blob from which, green-blue-red lines emerge describing the XY plane and the optical axis respectively. Tilted ~7° from the vertical, the optical axis is found to come closest to the most probable center positions of all the distributions when mapped onto an orbit radius of 740 nm. E. Circularly symmetrized densities of doublet orientations plotted on $\log_{10}$ scale (yellow bins) versus sin(θ) demonstrate the potential energy landscapes defining "up" state confinement at 15, 20, 40 mW powers. Numerous torque-free equatorial "transitions" (gray bins) distinguish the global equilibration at 15 mW (left panel) from tests of Brownian relaxation local to the "up" pole at 20, 40 mW (right-two panels). Yet continuous -$\sin^2(\theta)$ functions (black-solid curves in E) correlate well with densities (yellow bins) from both types of test. Moreover, the amplitude scale factors κ_U characterizing attraction to the "up" pole match the Boltzmann principle of energy equipartition, i.e. $\kappa_U = k_BT/\langle\sin^2(\theta)\rangle$, except when variances become un-resolvable at high power (≥ 75 mW). F. Parameterized by power, the diagram summarizes inner equilibration between "down","up" state populations plus global equilibration between the combined "down+up" state population and the rarified "transition state" as required to maximize entropy. Solid (red, green, blue) circles identify ratios derived from equilibrations at 8*, 10, 15 mW. Open-blue circles identify points set by the regression intercept P_D/P_U =1 at 7 mw. Open-blue star marks the regression intercept set by $P_D = P_U = P_{st}$ and $\kappa_{U/D} = 0$.

Footnote[3]: To initialize polarization state, the demon first sets a low laser power (~10 mW) allowing frequent doublet transitions between "up-down" hemispheres, then triggers a fast pulse of high power (e.g. ~100 mW) to detect and capture the desired polarization prior to further control.

2.4 Global equilibration and canonical thermodynamics

Fortunately, the region accessible to incident visible light imaging includes all of the "up" hemisphere plus a broad equatorial perimeter surrounding the microsphere. Thus, along with "up" state locations, nanoparticle position analysis also documents traverses in a nearly torque free region bridging "up"-"down" states at low powers. Collected and transformed to polar angle (θ) distributions (cf. Fig. 3E), the majority of locations map within an apparent microsphere profile and increase exponentially with power. At the same time, a smaller subset of nanoparticle locations map to the illuminated equatorial belt. Even more dramatic, this subset diminishes exponentially with increase in laser power. Lastly, too faint for pattern processing, the complement of images with nanoparticle locations in the "down" hemisphere reveal an even steeper exponential increase with power than in the "up" hemisphere. Thus, counted throughout trajectories with frequent "up"-"down" excursions, the demographics of high-speed images and patterns of nanoparticle orientations strongly support a coarse-grained three-state description of the global energy landscape. As exposed by demon bit maps in section 2.2, normalized occupancies of the three states provide experimental estimators [P_U, P_D, P_{ts}] for likelihoods of being in "up","down" states of strong polar attraction plus a broad equatorial state of rare-disordered "transitions". Viewed in the context of canonical thermodynamics, maximum entropy requires both inner equilibration between the "down","up" state populations plus global equilibration between the "down+up" state population and rarified "transition state". Hence, in Fig. 3F, we show the two power-dependent branches of free energy that characterize the globally equilibrated occupancies and emerge from independent breaks in symmetry.

3. BOLTZMANN THERMODYNAMICS

3.1 Photonic potentials in the "up" state

Lasting more than a minute, yet allowing no excursions to reach the "down" state, each 75s Brownian relaxation from the "up" state pole filled the "up" hemisphere region of attraction with ~$5x10^4$ nanoparticle positions. Even though kinetically trapped, the polar angle distributions acquired by relaxation at ≥ 20 mW exhibited the same "up" state dependence on polar angle as found for global equilibration at 15 mW, i.e. $\ln[\rho_U(\theta)] \approx \ln(\rho_U^o) - \kappa_U \sin^2(\theta)$. The obvious question to be addressed is can we consider the parameters κ_U and $\ln(\rho_U^o)$ to represent locally equilibrated "up" state distributions? More subtle than the question, we need to first define the domain of polar attraction to the "up" pole. Fortunately simple observation works here. Like the examples in Fig. 3E, the domain of polar attraction in all distributions was cut off at ≤ $\sin(\theta_U) \approx 0.8$. Equivalent to a circular radius of ~620-640 nm, the abrupt change in frequency of nanoparticle locations seems most likely to stem from increasing refraction of the scattered visible light as nanoparticle positions approach the rim of the microsphere. Thus, we expect the pattern shape to involve an implicit angle-dependent transfer function. Such a function can only be evaluated by tedious computations of the field equations[13-15] governing diffraction limited image formation and depends nontrivially on microsphere size. While useful for estimating microsphere dimension, what is most critical here for thermodynamic assay is that continuous records of images were processed throughout the orbit "up" latitudes and that all statistics were conserved. Hence, acting only as a bound to attraction, we use the observed the cutoff θ_U to define the domain of integration, leaving all density dependence on power to the field amplitude κ_U as shown by the density equation:

$$\rho_U(\theta) = \rho_U^o \exp\left\{\frac{-\kappa_U \sin^2(\theta)}{k_B T}\right\}$$

Expressed conveniently as a function of $\mu = \cos(\theta)$, we expose the normalization dependence on field amplitude by the integral,

$$1/\rho_U^o = \exp(-\kappa_U) \int_{\mu_U}^{1} d\mu \ \exp(\kappa_U \ \mu^2)$$

So to test local equilibration, we use the densities obtained by nanoparticle tracking (Fig. 3E yellow bins) to confirm that mean potential energies of attraction, $\kappa_U <\sin^2(\theta)>$, agree with Boltzmann's principle of energy equipartition for two (orbit rotational) degrees of freedom, i.e. 1 k_BT. First, we use slopes of regressions to ln(density) versus $\sin^2(\theta)$ to provide experimental estimates of the field amplitude κ_U, which notably yield excellent correlations (R values > 0.98) from 15 to 75 mW. Shown plotted versus beam power (Pwr) in Fig. 4A, the experimental estimates for field amplitude in the "up" state (solid green circles in Fig. 4A) increase linearly with power. Next confirming equilibration local to the "up" pole (cf. footnote below), we used the statistical variance $<\sin^2(\theta)>$ in each density distribution to predict the field amplitude κ_U following Boltzmann's principle of energy equipartition, i.e. $\kappa_U = k_BT/<\sin^2(\theta)>$. Also plotted in Fig. 4A versus beam power, the predicted field amplitudes are seen to agree well with the experimental estimates up to 50 mW. The amplitude then begins to deviate upward at higher powers where resolution in $<\sin^2(\theta)>$ diminishes.

3.2 Intensity field local to the trap

The polar attraction defines a circularly symmetric energy well that deepens progressively with increase in power. Referencing the potential to the torque-free region at the equator, the potential energy is described by,

$$E_U / k_B T \equiv \kappa_U [\sin^2(\theta_U) - \sin^2(\theta)]$$

Taking the derivative with respect to polar angle, we obtain the torque field $\tau_U(\theta)$ attempting to align the doublet with the optical axis -- albeit frustrated by entropy restriction, i.e.

$$\tau_U(\theta) \approx -4.1 pN \bullet nm \ [\kappa_U \sin(2\theta)]$$

The scale for torque is thermal energy k_BT and the field amplitude κ_U parameterized by dimensionless beam power Pwr. Proportional to $\sin(2\theta)$, the torque initially rises linearly as twice the polar angle (θ) then rolls over to peaks at 45^o. Scaled by $k_BT \approx 4.1$ pN nm and the maximum torque (amplitude $k_BT \ \kappa_U$) can be quite large. Based on the Rayleigh theory for small particle interactions with light[19,13], the principal contribution to rotational torque in our experiments is the gradient force created by induced dipole interactions with the laser electric field. Constrained to a trapped orbit (radius R_o) in a circularly symmetric intensity field, only gradients tangent to orbit circles connecting "up", "down" poles of the optical axis rotate the doublet, which connects force and torque to the derivative of intensity with respect to polar angle, i.e.

$$f_\theta \approx 0.5(\frac{n_w}{c})\alpha_p V_p (\partial I / R_o \partial\theta)_{orbit}$$

$$\tau_U(\theta) = R_o f_\theta \approx 3.3 pN \bullet nm \ (\partial I / \partial\theta)_{orbit} (nm^2 / nW)$$

Note: The force scale is parameterized by index of refraction for water $n_w \approx 1.33$, speed of light $c = 3x10^{17}$ nm/s, nanoparticle volume$V_p \approx 4.2x10^6$ nm^3, and the nanoparticle polarizability $\alpha_p \approx 0.353$ charactering polystyrene in water (Claussius-Mossotti relation[13]).

Thus, we acquire a thermodynamic assay for intensity field local to the "up" end of the trap beam waist and explicitly related to input power through κ_U (cf. Fig. 4A).

$$(\partial I/\partial\theta)_{orbit} \approx -1.24[\kappa_U \sin(2\theta)]nW/nm^2 \Rightarrow I(\theta)_{orbit} \approx 1.24\ \kappa_U[\sin^2(\theta_U) - \sin^2(\theta)]nW/nm^2$$

[Note: we neglect the small level of intensity at the orbit equator $I(\pi/2)_{orbit}$]. In the Conclusions section, we demonstrate that the assay.comes remarkably close to the putative power scale 0.44 Pwr mW.

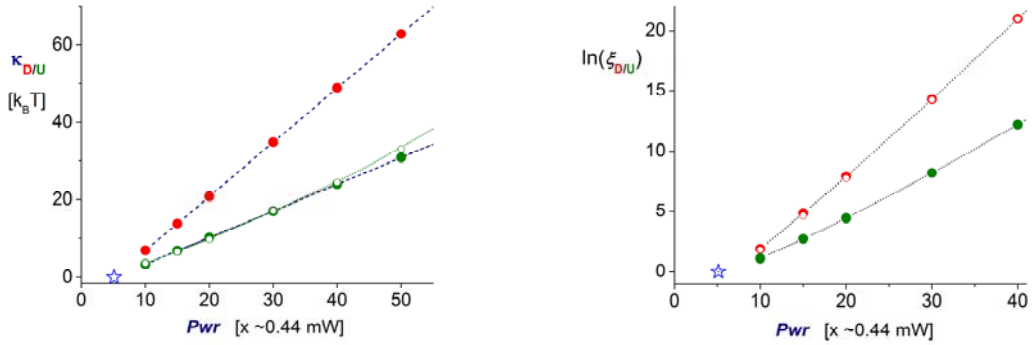

Figure 4. A. (left panel) amplitudes for "up" state potentials derived from analysis of nanoparticle position distributions appear in green (open and solid circles as described in text). Amplitudes for "down" state potentials derived from self consistent agreement with statistical weights appear in red.(solid circles) B. (right panel) "Up" state weights derived from experiments appear as solid-green circles and putative "down" state weights predicted by inner equilibration appear as solid-red circles. Open-red circles show the self consistent fit predicted by the "down" state potential amplitudes in A (left panel).

3.3 Self-consistent thermodynamic method to assay photonic potential in the "down" state

Central to canonical thermodynamics, entropy is maximized for a closed system containing a fixed set of states and the global sum $\Xi \equiv \Sigma_\chi\ \xi_\chi$ of local statistical weights,

$$\xi_\chi \equiv \int_{\mu\chi}^{1} d\mu\ \exp\left\{\frac{-E_\chi(\mu)}{k_B T}\right\}$$

In global equilibrium, the local weight for each state becomes scaled by its global probability P_χ to normalize density,

$$\rho_\chi^\Omega(\mu) = (P_\chi / \xi_\chi)\ \exp\left\{\frac{-E_\chi(\mu)}{k_B T}\right\}$$

and $\xi_\chi / P_\chi \equiv \Xi$ for all states. Thus, even though inaccessible to nanoparticle position tracking, we can use the ration P_D/P_U equilibrated at low powers to assay the "down" state weight given the canonical identity $\Xi = \xi_U / P_U = \xi_D / P_D$

rearranged to $\xi_D = \xi_U (P_D / P_U)$. Extended to enable self consistent evaluation at powers ≥ 15 mW, we show the putative "down" state weights plotted as solid-red circles along with "up" state weights derived from experiments plotted as solid-green circles in Fig. 4B. While unsubstantiated, our confidence in the extension to higher powers comes from the successful linear parametric scaling of "up" state potentials characterizing densities from 15 – 50 mW.

Turning now to the self consistent potential, we use a similar quadratic dependence on $\sin^2(\theta)$ (albeit with variable field amplitude κ_D and cutoff μ_D) found to well characterize "up" state orientations . Thus the trial weight ξ_D is defined by the barrier energy $\hat{E}_D / k_B T \equiv \kappa_D (1 - \mu_D^2)$ and density normalization $-\ln(\rho_D^o)$, i.e.

$$\xi_D = \exp(\hat{E}_D / k_B T) / \rho_D^o$$

Thus, analogous densities define "down" state confinement,

$$\rho_D(\mu) = \rho_D^o \exp\left\{\frac{-\kappa_D(1-\mu^2)}{k_B T}\right\}$$

and its normalization integral,

$$1/\rho_D^o = \exp(-\kappa_D) \int_{\mu_D}^{1} d\mu \ \exp(\kappa_D \ \mu^2)$$

all of which are defined by the trial field amplitude and cutoff angle.

Footnote: The normalization $1/\rho_U^o$ can be easily determine using an algorithm for "Dawson's Integral",

$$D(X) \equiv \exp(-X^2) \int_0^X dy \ \exp(y^2)$$

Superposed on the experimental estimates of "down" state weights in Fig. 4B, the open–red circles identify the self consistent agreement provided by the "down" state field amplitudes κ_D (solid-red circles in Fig. 4A). Importantly, we can use the self-consistent potential parameters to describe hidden "down" state distributions and the parameters fitting "up" state distributions to construct global energy landscapes as shown in Fig. 5 for powers from 7 – 20 mW. Moreover, we can derive the equilibrated free energy levels (short dashed horizontal lines in Fig. 5) to demonstrate the consequences of entropy confinement. Likewise, we can use the self-consistent parameters and similar thermodynamic assays to those in section 3.1 to estimate the photonic torque and intensity field in the "down" state region simply by substitution, i.e.

1) torque field aligning the doublet to the optical axis in the "down" state

$$\tau_D(\theta) \approx -4.1 pN \bullet nm \ [\kappa_D \sin(2\theta)]$$

2) self consistent thermodynamic assay for intensity local to the "down" end of the trap waist,

$$(\partial I / \partial \theta)_{orbit} \approx -1.24[\kappa_D \sin(2\theta)] nW/nm^2 \Rightarrow I(\theta)_{orbit} \approx 1.24 \ \kappa_D [\sin^2(\theta_D) - \sin^2(\theta)] nW/nm^2$$

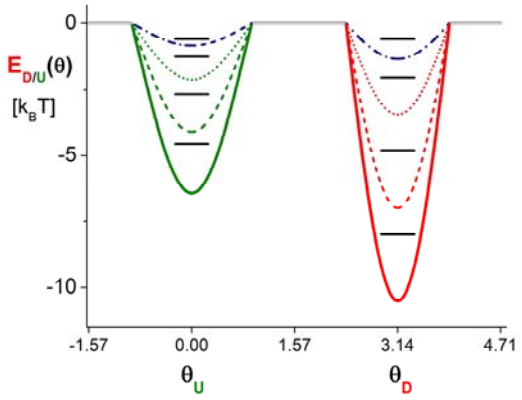

Figure 5. Potential energy landscapes found to characterize doublet attractions to "up" (green curves) and "down" (red curves) poles of the optical axis at powers of 10, 15, 20 mW . Short-horizontal lines mark the free energy level associated with each potential landscape. Also shown in dark blue are the landscapes predicted for 7 mW yielding identical free energy levels < 1 k_BT.

4. CONCLUSIONS

We verify that attaching a small Rayleigh-size particle to a micron-size sphere contributes imperceptibly to translational confinement in an optical trap when elevated far above the coverglass substrate. Yet, moved closer to the substrate, the appended nanoparticle is exposed by a significant power-dependent steric repulsion preventing close approach at high power. Recognized and cleverly managed, the demon selects a transient "up" - "down" orientation of the probe at low power and triggers a high power pulse to capture and align the probe in the desired polarization state. Remarkably, demon traces of repeated "up"-"down" transitions (bit maps) expose the origin of its success, i.e. the spontaneous break of "up"-"down" mirror symmetry driven by microsphere scattering in the trap. Moreover, the demon analysis enables a self consistent method to assay hidden "down" state potential energies of rotation and torques. Operating on the edge of thermal chaos at low powers, the demon senses an impending doom by revealing a putative critical point for "up" – "down" mirror symmetry at ~7 mW beam power (~ 3 mW in the trap). Even so, the trapping potential appears to vanish at ~0 power. Thus, we used nanoparticle tracking to examine the potential energy landscape governing rotation and its behavior at low power. Here, the field amplitudes characterizing polar attraction extrapolated to a lower beam power ~5 mW (~ 2 mW in the trap) – yet not zero – but consistent with a second symmetry break. Hence, assuming the estimated critical points are valid as well as the intercept for trap spring constants, it seems most likely that position fluctuations in the trap significantly renormalize (broaden) the trapping potential and randomize orientation.

We conclude by emphasizing that the induced dipole torque provides a photonic sensor to report laser intensity along the orbit encompassing the trap as well as its displacement from the trap center. To show this, we take the sensor scale for intensity (~ 1.25 nW/nm^2) and postulate a beam waist of ~ 500 nm appropriate[13] to our low filling ratio (cf. footnote[1]) to estimate the ratio of trap/beam power, which yields ~0.21 mW/Pwr near the "up" pole (x κ_U) and ~0.43 mW/Pwr near the "down" pole (x κ_D). Next, given the two-fold κ_D/κ_D ratio of potential amplitudes for "down" and "up" state pole attrctions, we can simply use solid angle divergence to estimate the hidden outward shift δZ relative to the trap center, i.e. $2.03 \approx (R_o + \delta Z)^2/(R_o - \delta Z)^2 \Rightarrow \delta Z \sim 175$ nm. Thus, supporting the outcome, values for both mW/Pwr and δZ are consistent with the results expected for a 1.2-1.3 μm sphere (cf discussion in footnote[1]). In regards to sensitivity of the thermodynamic assays, a 50% reduction nanoparticle size (e.g. to ~50 nm radius from 100 nm) would increase photonic sensitivity ~ten-fold (again without changing microsphere translational dynamics). At the same time, it would significantly increase the range of power allowing global equilibration from 15 to ~75 Pwr.

5. ACKNOWLEDGEMENTS

VB and IRK performed the experiments.VB developed the nanoparticle detection and pattern processing algorithms; IRK wrote the particle tracking and demon control software as well as programs to analyze the large data sets produced by the experiment. EE designed the experiment and worked out the statistical thermodynamics used to analyze the results. The authors thank Andrew Leung (University of British Columbia) for his help setting up the optical trap and developing the chemical methods needed to prepare particles. EE is grateful to Professor Cheng Zhu (Georgia Institute of Technology) for supporting this and other related projects through a NIH Subaward from his NIH grant (R01 AI044902-11). VB gratefully acknowledges fellowship support from the Dr. Ruediger Naumann-Etienne Foundation. Note: VB is currently at the MRC Laboratory of Molecular Biology, Cambridge CB2 0QH United Kingdom; IRK is currently at AIG, Wilton CT 06897.

6. REFERENCES

[1] Maxwell, J.C., "A dynamical theory of the electromagnetic field", Philosophical Transactions of the Royal Society of London **155**, 459-512 (1865).

[2] Vaikuntanathan, S. and Jarzynski, C., "Modeling Maxwell's demon with a microcanonical Szilard engine", Phys. Rev. E **83**, 061120 (2011).

[3] Horowitz, J.M. and Parrondo, J.M.R., " Thermodynamic reversibility in feedback processes", arXiv 1104.0332v1 (2011)

[4] Seifert, U., "Stochastic thermodynamics, fluctuation theorems and molecular machines", Rep. Prog. Phys. **75**, 126001 (2012).

[5] Raizen, M.G., "Demons, entropy and the quest for absolute zero", Sci. Am. **304**, 55-59 (2011).

[6] Berut, A., Arakelyan, A., Petrosyan, A., Ciliberto, S., Dillenschneider, R. and Lutz, E., "Experimental verification of Landauer's principle linking information and thermodynamics. Nature **483**, 187-189 (2012).

[7] Roldán, E., Martínez, I.A., Parrondo, J.M.R. and Petrov, D., "Universal features in the energetics of symmetry breaking", Nature Physics **10**, 457-461 (2014).

[8] Rowe, A.D., Leake, M.C., Morgan, H. and Berry, R.M., "Rapid rotation of micron and submicron dielectric particles measured using optical tweezers", J. Mod. Optics **50**(10),1539-1554 (2003).

[9] Bishop, A.I., Nieminen, T.A., Heckenberg, N.R. and Rubinsztein-Dunlop, H., "Optical microrheology using rotating laser-trapped particles", Phys. Rev. Lett. **92**(19), 198104 (2004).

[10] La Porta, A. and Wang, M.D., "Optical torque wrench: angular trapping, rotation, and torque detection of quartz microparticles", Phys. Rev. Lett. **92**(19), 190801 (2004).

[11] Arita, Y., Mazilu, M. and Dholakia, K., "Laser-induced rotation and cooling of a trapped micro gyroscope in vacuum", Nature Comm. **4**, 2374 (2013).

[12] Arzola, A.V., Jakl, P., Chvatal, L. and Zemanek, P., "Rotation, oscillation and hydrodynamic synchronization of optically trapped oblate spheroidal microparticles", Optics Express **22**(13), 16207-16221 (2014).

[13] Rohrbach, A. and E.H.K. Stelzer, E.H.K., "Optical trapping of dielectric particles in arbitrary fields. J. Opt. Soc. Am. A **18**(4), 839-853 (2001).

[14] Neto, P.A. and Nussenzveig, H.M., "Theory of optical tweezers", Europhys. Lett. **50**(5), 702 (2000).

[15] Mazolli, A., Neto, P.A. and Nussenzveig, H.M., "Theory of trapping forces in optical tweezers", Proc. Roy. Soc. Lond. A **459**, doi: 10.1098/rspa.2003 (2003).

[16] Neuman, K.C. and Block. S.M., “Optical trapping”, Rev. Sci. Instrum. **75**(9), 2787-2809 (2004).

[17] Mahamdeh, M., Campos, C.P. and Schäffer, E. 2011. “Under-filling trapping objectives optimizes the use of the available laser power in optical tweezers”, Optics Express **19**(12), 11759-11768 (2011).

[18] Kuznetsov, I.R. and Evans, E.A., “ Brownian nanoimaging of interface dynamics and ligand–receptor binding at cell surfaces in 3-D”, Methods **60**, 214-224 (2013).

[19] Harada, Y. and T. Asakura, T., “Radiation forces on a dielectric sphere in the Rayleigh scattering regime”, Optics Comm. **124**(5), 529-541 (1996).